NDT&E International 125 (2022) 102553

Contents lists available at ScienceDirect

NDT and E International

journal homepage: www.elsevier.com/locate/ndteint

Air leak detection in a pressurized containment building mock-up using elastic guided waves

Pierric Mora [a,*], Denis Vautrin [b], Guy d' Urso [b], Stéphane Letourneur [a], Mathieu Chekroun [a], Roberto Longo [a,c], Vincent Tournat [a]

[a] Laboratoire d'Acoustique de l'Université du Mans (LAUM), UMR 6613, Institut d'Acoustique - Graduate School (IA-GS), CNRS, Le Mans Université, France
[b] EDF R&D, PRISME Department, Chatou, France
[c] Groupe Signal Image et Instrumentation (GSII), Ecole Supérieure d'Électronique de l'Ouest (ESEO), 10 Boulevard Jeanneteau, 49107, Angers cedex 2, France

ARTICLE INFO

Keywords:
leak Test
Lamb waves
Noise correlation
Beamforming
VERCORS mock-Up

ABSTRACT

This article reports an experimental study of the vibrations induced by air leaks in realistic conditions reproducing a leak test of a containment building, such as those routinely conducted to probe the safety of nuclear power plants. The purpose of this work is to assess the effectiveness of a passive acoustic detection method that could assist and accelerate other scanning inspections. Using piezoelectric accelerometers, detection of leak signatures is demonstrated in the 0–20 kHz range. Noise correlation techniques are applied to obtain spectral power densities, maps of amplitudes and beamforming localization which correlate very well with the pressure applied inside the building and with the known locations and flow rates of the main leaks. At applied pressures of 4.2 bars and for concentrated leaks such as point breaks and decimeter long cracks, detection thresholds of about 500–600 L/h flow rates are reached at up to 4–5 m distance by accumulating data during 2 min under silent ambient noise conditions.

1. Introduction

Nuclear power plants are enclosed in a containment building designed to protect the reactor against external aggression and prevent radioactive steam from being released in the environment in case of an accident. In France, regulation [1] imposes to probe the quality of sealing every ten years by a leak test. During these tests, production is interrupted, the containment chamber is loaded at a static over-pressure of 4.2 bars and the overall leak rate is measured by monitoring pressure, humidity and temperature at different locations during 24 h. This measurement is known as *Integrated Leak Rate Test* - see Ref. [2] for a review focused on US standards and [3] for a comparison of French and British practices. Should this rate overpass a threshold of 1.125%[1] of the contained air mass per day - roughly 110 m^3/h, the reactor is not allowed to resume production until repairs are carried out and proved to be efficient in another leak test.

To date, EDF (french operator for nuclear power plants) routinely uses a method combining the spray of a soap solution and flow-meters to locate and quantify leaks, and decide where to perform mandatory or preventive repairs. This solution allows for very sensitive leak maps to be obtained, with a detection threshold around 10 L/h. However, as the entire wall surface needs to be scanned manually, this method results in time-consuming inspections involving several teams of operators. In view of limiting production interruption times and reducing the number of operators, rapid, automated alternatives are sought to assist the current procedure in locating the main leaks - typically above a few hundreds L/h, and within a couple meters tolerance for localization. EDF recently built a mock-up of a double walled concrete containment building, called VERCORS [4–7], as a 1:3 scale specimen representative for 24 (about 40%) of the french reactors. The purpose of this mock-up is to study the aging of the inner wall and follow the evolution of the leak rate consecutive to drying creep and loss of pre-stress, in a realistic environment. In this context, the present work explores the applicability and performance of an acoustic detection method on leak tests realized at VERCORS.

In the past, passive leak detection techniques using acoustic waves

* Corresponding author.
E-mail address: pierric.mora@univ-eiffel.fr (P. Mora).

[1] legal threshold in France for the inner chamber of double-walled buildings, representing an acceptance limit of 1.5% in an accident scenario with a safety factor of 1.3. For 900 MW simple-walled buildings the acceptance limit is 0.162% (0.3% in an accident scenario).

https://doi.org/10.1016/j.ndteint.2021.102553
Received 4 November 2020; Received in revised form 8 September 2021; Accepted 5 October 2021
Available online 13 October 2021

received much attention for their potential to inspect or monitor pipe networks supplying water [8–10], high-pressure gas [11,12], etc. Indeed, in such 1D guiding structures, low-frequencies generated by the turbulent flow escaping through the leak (typically $0-500$ Hz in the mentioned references) can propagate almost without attenuation over long distances, and localization can easily be done by cross-correlating two synchronized sensors placed at either sides of the leak. For example, Fuchs and Riehle [8] reported large measurement campaigns on water supply networks reaching leak rate detection thresholds as low as 50 L/h with 90% successful localization rate on pipeline sections up to 250 m long. Colombo et al. [13] reported increased detection ranges over 1 km sensor separation for larger leaks using active acoustic measurements.

In plate-like structures however, long range detection is hindered by the 2D geometric decrease (as $1/\sqrt{r}$ in amplitude) which dominates attenuation at low frequencies. Localization methods must resort to more measurement points, either by finely meshing the surface to produce amplitude maps, or by using arrays of sensors to determine the direction of origin of signals through beamforming processing. Applications were proposed by Holland et al. [14–16] to detect air leaks caused by micrometeorite or debris impacts in a spacecraft, with reported meter long detection ranges at $200-600$ kHz. Moriot et al. [17] used beamforming techniques to detect small leaks from a noisy background in a mock-up representing a steam generator unit of a nuclear reactor. When the propagation medium is more complex than a simple scalar medium, these array processing techniques are often called "Matched Field Processing" in oceanography and geophysics, after Bucker's [18] introductory work in the late 70s (see Refs. [19,20] for reviews, Ref. [21] for a recent application to locate weak noise sources during extraction at a hydrocarbon field, Ref. [22] for an application to locate events in concrete structures, or Refs. [23,24] for defect localization in a reverberating medium). Improving those processing under challenging conditions (low signal-to-noise ratio, coherent multiple sources, few receivers, limited knowledge on the medium, *etc*) is still an active research area, with recent developments based on compressed sensing [25,26] or machine learning [27,28]. Along with other tools such as inversion of subsurface velocity maps from reconstructed Green's functions [29–32], they are a way of extracting information from ambient noise correlations.

The objective of the present work is to quantify the feasibility of a passive acoustic detection method in terms of detection range using commercially available, low-noise sensors. The major challenge is to deal with signals that are often weaker than the instrumental noise, and are sometimes contaminated with ambient noise. The experimental material reported in this article splits into two steps which were realized during the 03/2018 and 03/2019 leak tests at VERCORS, under realistic conditions. The first step focuses on the detectability of leak signals in the 0–20 kHz range using broadband piezoelectric accelerometers, which were placed at various distances from known leaks. The second step focuses on the performance of beamforming processing using small antennas, placed near one specific leak, in the context of multi-modal propagation and heterogeneities. After describing the experimental setup, giving the wave propagation characteristics in the inner wall, and defining the signal processing tools, the results of both experiments are analyzed and conclusions for future prospects are drawn.

2. Description of the experiment

2.1. Overview

At day 1 a compressor injects air inside the internal chamber until reaching an over-pressure of 2 bars, stops during 2 h, and then starts again until reaching an over-pressure of 4.2 bars (*i.e.* the absolute pressure at this final step is 5.2 bars). It takes around one day to get to this step. Due to the pressure gradient between both chambers, air may leak wherever the wall is cracked or porous enough. The air flows emit weak and constant whistles which are recorded by vibration sensors placed at different locations on the external face of the chamber. After 12 h the pressure starts being released and it takes another 15–20 h to get back to atmospheric pressure. The time history of this loading and unloading is schemed in Fig. 1-(a), -(b) and -(c). Short before start and during both 2 bars and 4.2 bars steps all loud devices such as compressor, inter-chambers ventilation, temperature and humidity regulators are turned off, ensuring a very silent background above 1 kHz. The 4.2 bars step is shared with other teams which perform active experiments or penetrate inside the inter-chambers space, but the resulting acoustic contamination is easily detectable as it is transient. Besides, the inter-chambers space is closed at the beginning and end of the 4.2 bars step, times during which it is easy to record very long signals with excellent background conditions.

2.2. Sensor locations and data acquisition

The 2018 and 2019 experiments involved different sensor locations. In 2017 the map of leaks was determined using soapy water for detection and flowmeters for quantitative measurements, showing that the main leaks concentrate in two regions (see Fig. 1-(b) and -(d)). The first region corresponds to the gusset, *i.e.* the circumferential part of the wall located immediately above the base slab, between -0.3 m and -1 m altitude, which is thicker (0.6 m thickness) than the rest of the wall (0.4 m thickness). The second region is around an access door at the center of the wall and has only two significant leaks higher than 150 L/h at 4.2 bars. The door is sealed in a concrete reinforcement which makes the wall thicker (about 0.5 m thickness) in an area of side length 4.8 m – the reinforcement is polyhedral, so that the 0.1 m over-thickness slightly varies and the step does not follow perfectly the curvature of the wall.

Based on this knowledge, in the 2018 experiment the sensors were distributed in several regions (see Fig. 1-(d), crosses): 8 points were placed close to the central door, with min − max distances to a strong punctual leak of 0.55 m (A31 point) to 5.1 m (A44 point), while 8 other points divided into two subgroups of 4 were placed far from the central door but close to the leaks at − 1 m altitude (A1*i* points) and far from any strong leak (A2*i* points).

In the 2019 experiment the sensors were distributed in three independent groups of 8 points (see Fig. 1-(d), dots, and -(e)) arranged in circular arrays with a radius of 0.12 m, and placed at a distance of 1.7 m–2 m from the strong punctual leak.

The values of flow rates reported in Fig. 1-(d) and everywhere else in this article correspond to the 2018 survey and were measured at 4.2 bars. The general trend over years is an increase of these rates. In 2019, the global leak rate had increased from 46.2 ± 0.9 m^3/h to 57.1 ± 1.2 m^3/h, *i.e.* around +25% - the reader should have this information in mind when comparing both experiments.

In either experiment the acquisition chain is as follows. The sensors are piezoelectric, broadband accelerometers Bruel & Kjaer type 4370 with mounted resonance frequencies[2] measured at 12–13 kHz (major), $18-19$ kHz (minor) and $22-23$ kHz (major). They are screwed to mounting studs, which are themselves epoxied to the wall. Bruel & Kjaer type 2692-A-0S4 Nexus signal conditioners are used at sensitivity 316 V/g, where $g = 9.81$ m/s^2 is the standard acceleration due to gravity, and set to band-pass the 10 Hz − 30 kHz range. Low-noise cables 5 m long are used to connect the sensors to the conditioners. Digitization at 14 bits is performed on independent 8-channels stations made of two synchronized 4-channels TiePie USB oscilloscopes, at a sampling frequency of 100.8 kHz. The instrumental noise of the entire chain is essentially white in the band 100 Hz − 50.4 kHz, and has a measured root mean square amplitude of 0.025 mV, which converted in acceleration gives 8×10^{-8} *g*. This noise floor is used to define the 0 dB level. 1.3 s long

[2] The vendor specification is 16 kHz, but this value must be considered as indicative due to the strong influence of coupling.

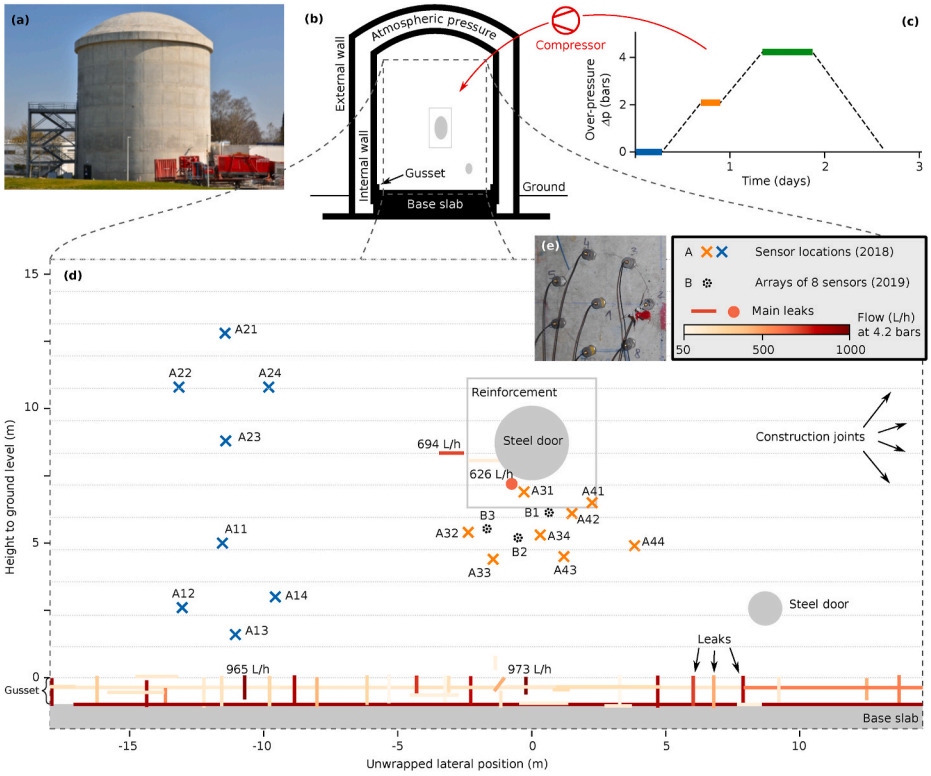

Fig. 1. Scheme of the experiment. (a) Photograph and (b) scheme of the VERCORS mock-up. (c) Time history of the pressure proof of the internal chamber. (d) Map of the internal wall (exterior side) indicating the main inhomogeneities, main leaks (flow rates from the 2018 survey), and accelerometer locations for the 2018 and 2019 experiments. (e) Photograph of an accelerometer array of the 2019 experiment.

signals are periodically recorded and stored. In Fig. 1-(d) the 2018 points sharing the same color (*i.e.* A1i − A2i on the one hand and A3i − A4i on the other hand) where recorded synchronously. The three 2019 arrays have three independent clocks.

2.3. Preliminary characterization of Lamb waves propagation in the internal wall

At the operating frequencies, *i.e.* between 2 kHz and 20 kHz, for a wall thickness $d = 0.4$ m, longitudinal speed $c_L \approx 5.4$ m/ms and shear speed $c_S \approx 2.6$ m/ms, the frequency-thickness products range between $0.15 \leq fd/c_L \leq 1.5$ and $0.31 \leq fd/c_S \leq 3.1$, meaning that wave propagation can be well described with Lamb waves [33]. The equipment described in the former paragraph was used to measure the dispersion relations in the internal wall: 16 accelerometers were arranged in a row with a periodic spacing of 0.2 m to record the transient motion produced by an impact located in the alignment of the row. The results of this characterization are represented in Fig. 2 in the form of a $p - \omega$ transform (see Ref. [34], a detailed analysis of the artifacts[3] can be found in Ref. [35]), together with an adjusted theoretical model calculated with a Young's modulus $E = 45$ GPa, Poisson's ratio $\nu = 0.35$ and mass density $\rho = 2500$ kg/m^3. The model was obtained by targeting the A_0 mode and setting the weakly constrained parameters (c_L and ρ) to plausible values. Three frequency regions can be distinguished regarding the surface motion: a low frequency region up to about 4 kHz where the out-of-plane component is mostly due to the lowest order antisymmetric mode A_0, then an intermediate region up to about 10 kHz where several modes contribute on similar proportions, and finally a high frequency region where higher order modes have negligible contributions in the far field compared to the Rayleigh (surface) wave.

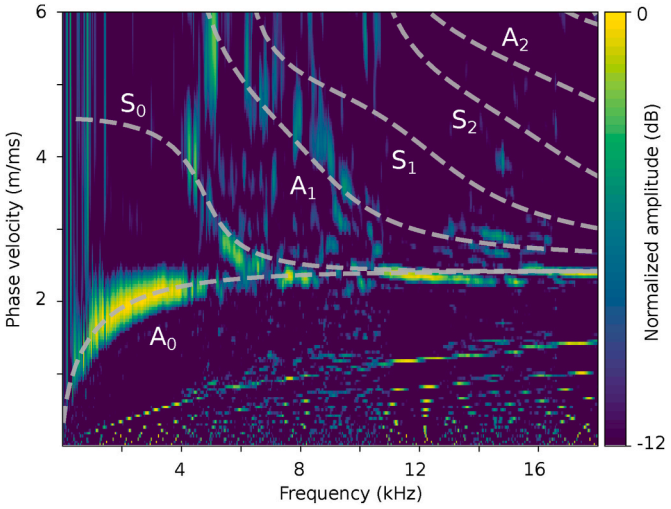

Fig. 2. Dispersion curves of Lamb waves in the internal wall obtained from active measurements. Dashed lines represent an adjusted model of a homogeneous wall with thickness $d = 0.4$ m, mass density $\rho = 2500$ kg/m^3, Young's modulus $E = 45$ GPa and Poisson's ratio $\nu = 0.35$.

3. Data processing

3.1. Preliminary view of time signals

The 8 signals sharing a common clock are stored in a vector called $\mathbf{s}(t) = (s_1(t), \ldots, s_8(t))^T$ in the time domain. The discrete Fourier transform of the signal vector is called $\mathbf{S}(f) = \mathcal{F}\{\mathbf{s}\}(f)$. A typical record for a

[3] such as the thin curves below the A_0 mode, which are due to spatial aliasing, or the vertical lines at low frequencies, due to a decreasing resolution.

sensor located near a leak is presented in Fig. 3 (point A31, distant of 0.55 m from a punctual leak flowing at 626 L/h at 4.2 bars). It is shown that despite signals look stochastic over a few dozens milliseconds, their spectra are constant over hours, which allows for accumulation of correlations on long times. As one would expect, a dependence with pressure can be observed; this is particularly visible around 5 kHz and 23 kHz. The latter peak is due to a resonance of the sensor. The former is a strong out-of-plane response of the wall as a result to several specific modal contributions: in addition to the A_0 mode, the (propagating) S_0 mode acquires a significant out-of-plane component while entering its dispersive region, and two near-field effects caused by the $S_1 - S_2$ Zero-Group Velocity (ZGV; see *e.g.* Refs. [36–38]) point and the S_1 cutoff are strongly observed because of the proximity of the leak. One can also notice several rays in the spectrograms: the ones at 13 kHz, 19 kHz and 22 kHz are due to resonances of the sensor, while most of the others are likely due to cutoff frequencies of longitudinal type (*i.e.* those having a pure out-of-plane motion) as they match well with a theoretical sequence $f_n = nc_L/2d$, with $d = 0.5$ m (the wall is thicker in this area) and $c_L \approx 5$ m/ms. Finally, an aspect of major concern is the weakness of the raw signals: despite the low-noise and high-sensitivity quality of the acquisition chain, and except from the 5 kHz and 23 kHz peaks where the signal to noise ratio (SNR) is about 8–10 at 4.2 bars, most of the spectrum has a SNR around or below 1 at maximum pressure and close distance. Therefore, without a sufficiently long averaging of

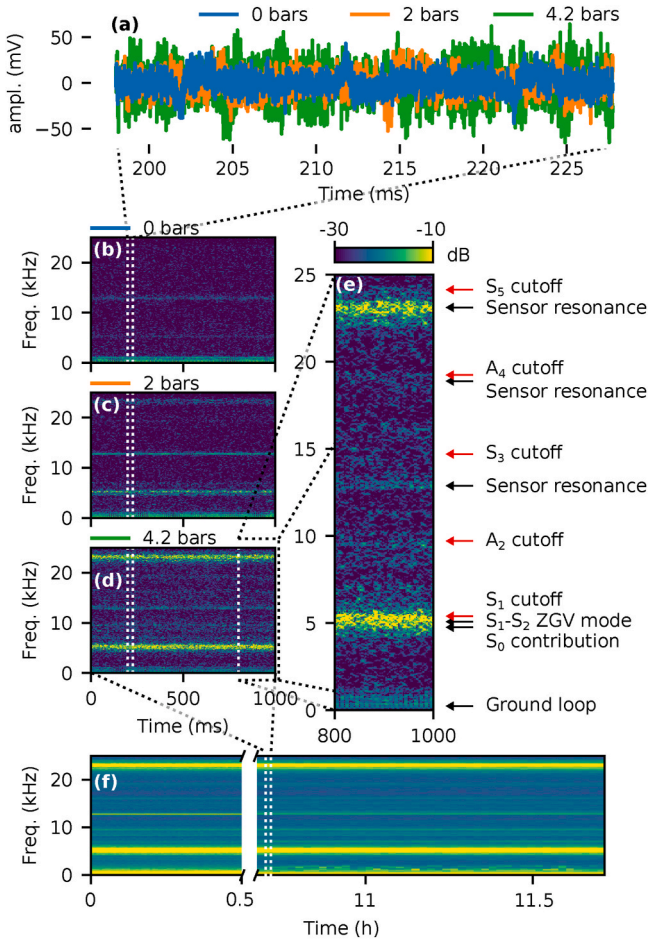

Fig. 3. Typical signals near a leak (A31 point): (a) raw signals, and associated spectrograms corresponding to an over-pressure inside the internal chamber of (b) 0 bars, (c) 2 bars and (d, e) 4.2 bars. (e) Red arrows indicate theoretical cutoff frequencies $f_n = nc_L/2d$ of longitudinal kind for a wall with thickness $d =$ 0.5 m and long. wave speed $c_L \approx 5$ m/ms (f) 1 s-averaged spectra at 4.2 bars over hours. (For interpretation of the references to color in this figure legend, the reader is referred to the Web version of this article.)

correlations, which requires excellent ambient noise conditions, the range of detection for $\propto$ 500 L/h leaks is as short as a few dozen centimeters. The purpose of the next paragraphs is to show how this range can be enhanced using long time histories.

3.2. SNR enhancement by accumulation of correlation functions on long records, and reference subtraction

As will be seen further, although the signals are very weak, the dominant source of noise in the experiments above 1–2 kHz is not of anthropic or environmental origin, but is due to the electronic noise of the sensors and acquisition chain. The 2018 experiment also suffered another source of contamination, but this is the topic of a subsequent paragraph.

Let us model the measured signal vector $\mathbf{s}(t) = \mathbf{q}(t) + \mathbf{n}(t)$ as a sum of a genuine source signal $\mathbf{q}$ and a noise term $\mathbf{n}$. The noise term describes the instrument noise, *i.e.*, the electronic noise of each sensor connected to the acquisition chain (essentially white noise in the 100 Hz − 50.4 kHz range, see Sec. 2.2). It is not coherent between distinct sensors, and its power density is constant during the entire experiment. $\mathbf{q}$ and $\mathbf{n}$ are both stochastic signals, and are uncorrelated. The data covariance matrix is given by:

$$\mathbf{K}(f) = \langle \mathbf{S}\mathbf{S}^H \rangle. \tag{1}$$

In Eq. (1), $.^H$ means hermitian transpose, and $\langle . \rangle$ refers to an averaging over different time segments. In this work, long records are split into detrended, Hann-windowed 10 ms long segments with 50% overlapping.

Ideally, for an averaging on infinitely long times one should have $\mathbf{K} = \langle \mathbf{Q}\mathbf{Q}^H \rangle + \langle \mathbf{N}\mathbf{N}^H \rangle$, with $\mathbf{Q} = \mathcal{F}\{\mathbf{q}\}$ and $\mathbf{N} = \mathcal{F}\{\mathbf{n}\}$, and $\langle \mathbf{N}\mathbf{N}^H \rangle = \mathrm{diag}(|N_i|^2)$. Indeed, due to uncorrelation, cross terms $\langle \mathbf{Q}\mathbf{N}^H \rangle$ and $\langle \mathbf{N}\mathbf{Q}^H \rangle$ average to zero. It is assumed that the ambient noise conditions previous to the beginning of the pressure increase are good enough such that recording at the 0 bars step yields an accurate characterization of the instrument noise, *i.e.* $\mathbf{K}_{(0\ \mathrm{bars})} = \langle \mathbf{N}\mathbf{N}^H \rangle$. The result of subtracting this reference is stored in the matrix

$$\mathbf{K}_d = \mathbf{K} - \mathbf{K}_{(0\ \mathrm{bars})} \tag{2}$$

and called "de-noised" covariance matrix. However, as the accumulation is performed on a finite number of time segments (say, M segments), fluctuations of the order of $(|N|^2 + 2|N||Q| + |Q|^2)/\sqrt{M}$ contaminate diagonal and off-diagonal terms of $\mathbf{K}$, where $|N|$ and $|Q|$ are the average noise and average signal densities. The SNR for cross-spectral terms $\sqrt{K_{i,j,i\neq j}}$ is therefore expected to increase proportionally to $M^{1/4}$. The same convergence can be expected for diagonal terms $\sqrt{K_{i,i}}$, provided that the average noise density is first subtracted.

Contrarily to $\mathbf{K}$ whose invertibility is ensured by $\langle \mathbf{N}\mathbf{N}^H \rangle$, $\mathbf{K}_d$ may tend to a singular matrix, with eigenvalues fluctuating around zero for a finite number of averages. This feature should be kept in mind for an application of super-resolution beamforming methods which use this inverse of the data covariance matrix.

The upper discussion is illustrated in Figs. 4 and 5. The former focuses on the off-diagonal terms of $\mathbf{K}$ and is relevant in the context of the 2019 data only, as information from inter-sensor correlations was ignored in the 2018 experiment. The latter is relevant for both data sets.

In Fig. 4 correlograms are represented in the time domain (*i.e.* after performing an inverse discrete Fourier transform) and frequency domain, showing the improvement of the noise floor on off-diagonal terms of $\mathbf{K}$ as the recording time increases: up to 20 dB are gained for 2 min stacking. Cross-correlations with sensor 1 were arbitrarily selected for the figure to illustrate the behavior of all terms, but the following analysis does not depend on this choice as it takes into account the entire correlation matrix.

In Fig. 5 correlograms are represented in the frequency domain,

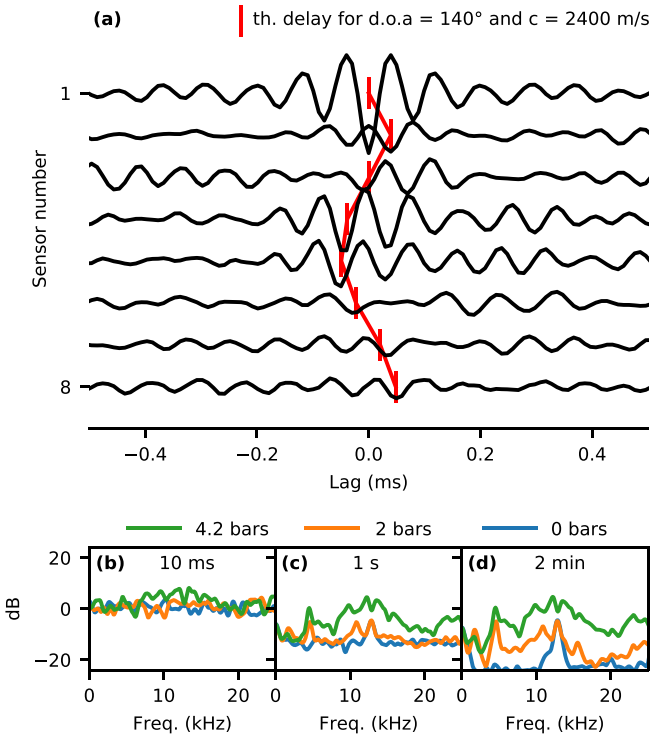

Fig. 4. Noise correlation functions for array B1 with central element (number 1) as reference. (a) Time domain correlations on 10 ms segments for 2 min stacking, at 4.2 bars. Red bars represent theoretical inter-sensor delays for a direction of arrival of 140°, *i.e.* pointing towards the closest leak, and a wave speed of 2400 m/s, *i.e.* corresponding to a Rayleigh wave. (b), (c), (d): Frequency domain correlation of sensors 1 and 8, for several stacking duration, corresponding to (b) 1, (c) 10^2 and (d) $\sim 10^4$ segments. Curves are low-pass liftered using cepstrum editing [39] for smoother rendering. (For interpretation of the references to color in this figure legend, the reader is referred to the Web version of this article.)

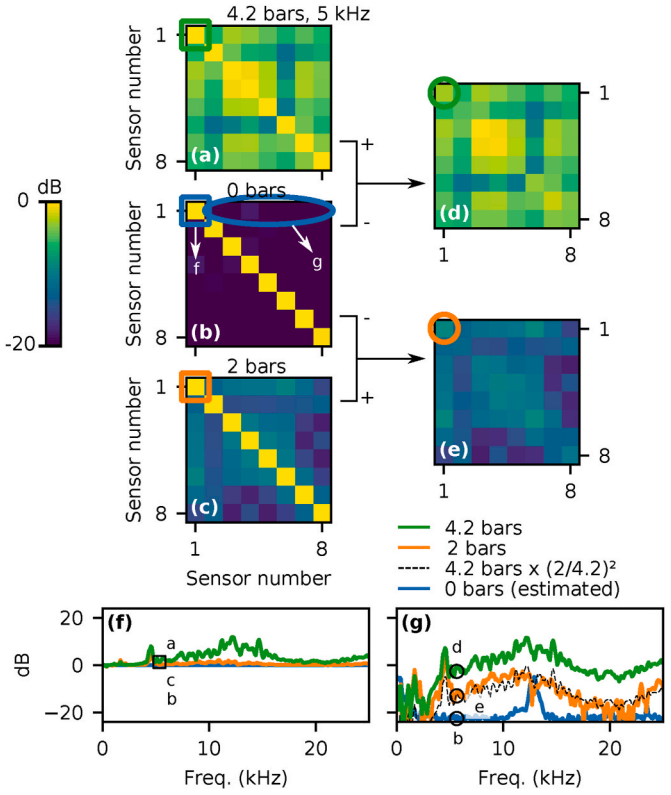

Fig. 5. Illustration of SNR enhancement for auto-correlations by reference subtraction. (a), (b) and (c): 2 min stacked correlation matrix of the B1 array at 5 kHz. (d) and (e): de-noised matrices. (f) and (g): spectrum measured by the central sensor (f) without and (g) with de-noising. The improved noise floor ((g), 0 bars) is estimated as the average off-diagonal correlations with sensor 1.

showing the improvement of the noise floor on diagonal terms of $\mathbf{K}_d$. The reference level at 0 bars is therein estimated as the average of off-diagonal terms rather than from another data set. Fig. 5-(g) also shows that the relation between pressure gradient and acoustic amplitude matches well a quadratic law $\|\mathbf{q}\| \propto \Delta p^2$ in the entire measurement range, as the spectrum at 4.2 bars divided by $(4.2/2)^2$ (dashed black curve) almost fits the spectrum at 2 bars (solid orange curve). All dB units in Figs. 4 and 5 and further are power-dB with respect to the reference noise density level, *i.e.* 10 $\log_{10}(./|N|^2)$, which corresponds to an amplitude of 0.025 mV (see Sec. 2.2).

3.3. Subtraction of AC-driven background noise specific to the 2018 experiment

When applied to the signals of the 2018 experiment, the above described procedure reaches a disappointingly high limit for the noise floor: For most points, all 0 bars, 2 bars and 4.2 bars steps reveal a background noise of −10 dB to −3 dB which overshadows the signature of the leaks. An example of this background is shown in Fig. 6-(b) which represents the correlation matrix of 8 accelerometers at an arbitrary frequency, at the 0 bars step: in ideal conditions the only noise should be instrumental and this matrix should be purely diagonal, which is obviously not the case here. Fortunately, this contamination has a distinctive feature which enables filtering it out: a time-frequency analysis shows a repeated pattern with a repetition rate of 20 ms (see Fig. 6-(a) where, because of the absolute value, the rate appears to be of 10 ms), characteristic of an AC-supplied device. This background noise is not perfectly constant over hours, but is periodic enough on short periods such that this property can be exploited.

Contaminated signals $\mathbf{s}(t) = \mathbf{q} + \mathbf{b} + \mathbf{n}$ can hence be modeled with an extra contribution, called $\mathbf{b}(t)$, which represents a mechanical vibration and can be correlated between two different sensors, but is uncorrelated to $\mathbf{q}$ and $\mathbf{n}$ and is such that $\mathbf{b}(t + 20\text{ ms}) \approx \mathbf{b}(t)$. Under the additional hypothesis that $\mathbf{q}(t + 20\text{ ms})$ and $\mathbf{n}(t + 20\text{ ms})$ are uncorrelated to $\mathbf{q}(t)$ and $\mathbf{n}(t)$, de-contamination can be achieved by substituting $\mathbf{s}(t)$ with

$$\widetilde{\mathbf{s}}(t) = \frac{\mathbf{s}(t) - \mathbf{s}(t + 20\,\text{ms})}{\sqrt{2}} \tag{3}$$

in Eqs. (1) and (2) to construct $\mathbf{K}$ and $\mathbf{K}_d$. In Eq. (3) the $2^{-1/2}$ normalization factor ensures that $\langle \widetilde{\mathbf{S}}\widetilde{\mathbf{S}}^H \rangle = \langle QQ^H \rangle + \langle NN^H \rangle$.

The effect of this pre-treatment is illustrated in Fig. 6. Firstly, it can be appreciated on records at 0 bars that the repetitive pattern (Fig. 6-(g)) and the abnormal non-zero cross-correlations (Fig. 6-(h)) modeled by the **b** term have disappeared and that the theoretical noise floor is indeed reached (about −20 dB for off-diagonal terms in this case of a stacking over 2 min, see Sec. 3.2). Two highly contaminated points (A13 and A32) are taken as examples in Fig. 6-(i) and -(j) to show the benefits on leak signals. Finally, two "gold standard" examples are given in Fig. 6-(k) and -(l) to prove that no relevant signal component has been removed: Fig. 6-(k) shows point A22 which is of weak intensity and weakly contaminated, and Fig. 6-(l) shows point A31 whose intensity is strong enough to emerge from contamination.

3.4. Beamforming: Delay and Sum (D&S)

Two methods to locate sources from the inter-phases measured in an array of sensors are applied to the signals of the 2019 experiment. Both rely on a precise knowledge of the sensor locations and on a propagation

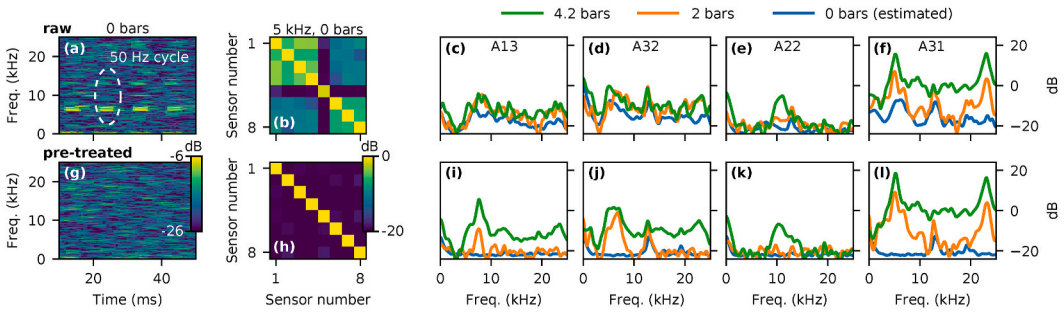

Fig. 6. Illustration of the pre-treatment $s(t) \to 2^{-1/2}(s(t) - s(t + 20\text{ ms}))$ specific to the 2018 experiment, which suffered from AC-driven background noise. First row ((a) to (f)) is raw data and second row ((g) to (l)) is pre-treated data. (a) and (g): spectrogram of a typical contaminated signal showing (a) a 20 ms pattern, (b) and (h): 2 min stacked correlation matrix of A3i − A4i points at 5 kHz showing (b) ab-normal non-zero off-diagonal terms at 0 bars, (c) to (f) and (i) to (l): spectra of several points normalized by the average sensor noise floor, processed with 2 min stacking of correlations on 10 ms segments, and reference subtraction. Curves are low-pass liftered using cepstrum editing [39] for smoother rendering. 0 bars curves are estimated from off-diagonal correlations.

model, which is here cast in the frequency domain and includes a far field hypothesis by assuming plane wave arrivals on the array.

The first method is often called "Delay and Sum", or "Bartlett's beamforming" [40,41], and consists in summing signals with weights which correct theoretical inter-sensor phase delays for a source in the test direction. The maximums of the power-amplitude of such sum signal as a function of test direction indicate the locations of sources. For two given frequency bounds f_1 and f_2, this power-amplitude is defined as:

$$P^{(\mathrm{D\&S})}(\theta) = \sum_{f_1}^{f_2} \mathbf{A}^H \mathbf{K}_d \mathbf{A}, \tag{4}$$

where

$$\mathbf{A}(\theta, f) = \left(\mathrm{e}^{2i\pi f \tau_1}, \ldots, \mathrm{e}^{2i\pi f \tau_8}\right)^T \tag{5}$$

is the steering vector,

$$\tau_i(\theta, f) = \frac{\mathbf{e}_\theta^T \mathbf{r}_i}{c(f)} \tag{6}$$

is the ith time delay, $\mathbf{e}_\theta^T$ is a unitary vector pointing in the test direction θ, $\mathbf{r}_i$ is the position of the ith receiver and c is the phase velocity of the propagation model. Usually, $\mathbf{K}_d$ is whitened before applying Eq. (4) to prevent the outcome from being dominated by spurious frequencies.

D&S is a linear method, relatively robust to low SNR and moderate knowledge of the model. However, its angular resolution is limited by the ratio of the wavelength over the inter-sensor spacing and thereby gives poor performance at low frequencies.

3.5. Beamforming: Minimum Variance Distortionless Response (MVDR)

The second method used in this work is usually called "Minimum Variance Distortionless Response", or "Capon's beamforming" [42]. MVDR is a non-linear technique whose resolution is limited by the SNR and is able to resolve subwavelength details. On the other hand, it is more critically sensitive to the accuracy of the propagation model and knowledge of the sensor locations than D&S. In this technique the weights to build the sum signal depend on the inverse of the covariance matrix such that the power at a given test direction reads:

$$P^{(\mathrm{MVDR})}(\theta) = \sum_{f_1}^{f_2} \frac{1}{\mathbf{A}^H \mathbf{K}_d^+ \mathbf{A}}. \tag{7}$$

In Eq. (7) $\mathbf{K}_d^+$ is a pseudo-inverse inspired from the Moore-Penrose pseudo-inverse. One resorts to a pseudo-inverse rather than a true inverse because, as explained before, $\mathbf{K}_d$ may fluctuate around a singular matrix due to the subtraction of the reference covariance matrix. Given the eigen-decomposition $\mathbf{K}_d = \mathbf{U}\,\mathrm{diag}(\sigma_i)\,\mathbf{U}^H$, a way to define a pseudo-inverse is:

$$\mathbf{K}_d^+ = \mathbf{U}\,\mathrm{diag}(1\,/\,(\varepsilon + |\sigma_i|))\,\mathbf{U}^H. \tag{8}$$

In Eq. (8), ε is a parameter which separates meaningful eigenvalues from noise. Its value is chosen proportionally to the estimated noise density: $\varepsilon(f) = |N|^2/4$, where $|N|^2$ is the average of off-diagonal terms of $\mathbf{K}_{(0\text{ bars})}$. Note also the absolute value in $|\sigma_i|$ to ensure invertibility. As for D&S, $\mathbf{K}_d$ is whitened before applying Eq. (7).

The choice between D&S and MVDR must be made according to the frequency range and SNR. At low frequencies, MVDR can be a very powerful alternative to D&S to enhance contrasts. However, D&S is more suited to the intermediate frequency range 4 kHz–10 kHz where the out-of-plane surface motion is multimodal, or to lower pressures and higher frequencies where the SNR is worse.

4. Results and discussion

4.1. Analysis of the 2018 experiment

The results of the 2018 experiment are processed according to Eqs. (1)–(3) and represented in Fig. 7. Maps of amplitudes integrated in two frequency ranges and interpolated between the measurement points within each set are shown. Additionally, the spectrum measured by each sensor is drawn nearby its corresponding location for all pressure steps. The spectra at 4.2 bars divided by $(4.2/2)^2$ are also drawn (dashed black lines) in order to compare them with the 2 bars step and evidence a relation of the kind amplitude $\propto (\Delta p)^2$.

First of all, the intensity maps are overall consistent with the survey performed independently using soapy water for detection and flowmeters for quantification: the highest amplitudes are measured in the neighborhood of the central access door (A3i − A4i points) and near the highly leaking region at − 1 m altitude (A1i points), whereas points far from significant leaks (A2i points) recorded the weakest signals. The 0–10 kHz intensity map (Fig. 7-(a)) is dominated by the A31 point, but this is mostly due to a very high peak at 5 kHz which is probably in part due to the contributions of the S_1 cutoff and $S_1 - S_2$ zero-group velocity mode, *i.e.* near field effects, while weaker signals are also unambiguously detected on other points. The 10–20 kHz intensity map (Fig. 7-(b)) shows more balanced levels.

Consistency with the pressure gradient can also be observed except for the weakest points where the 2 bars step produces undetectable low signals. The relation between amplitude and pressure appears to follow reasonably well a quadratic trend over the entire data set. This non-linear behavior is a drawback for the reliability of detection and in view of flow estimation based on the acoustic intensity, because a single leak is expected to radiate amplitudes twice higher than two half-weaker leaks together. It is therefore expected that this detection method is more sensitive to punctual leaks or concentrated leaking regions than

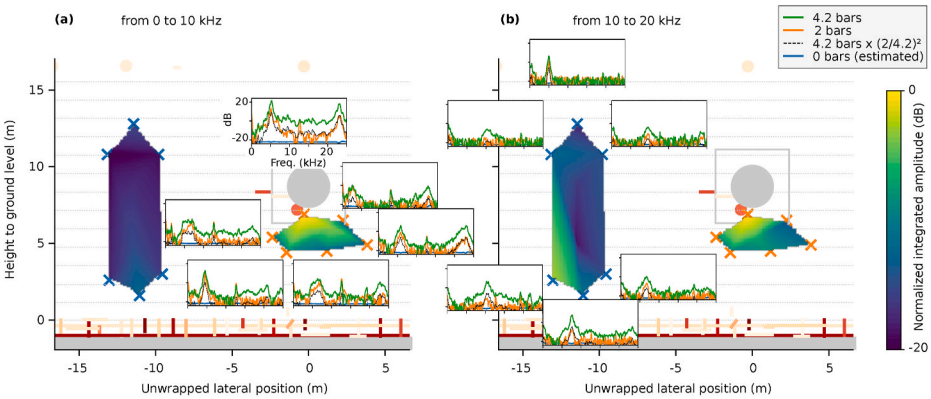

Fig. 7. Results of the 2018 experiment: color-maps of spectral amplitude at 4.2 bars integrated in the (a) $0-10$ kHz and (b) $10-20$ kHz ranges. Red lines and circles represent the main leaks; their colorscale is proportional to their flow rate (see Fig. 1). (For interpretation of the references to color in this figure legend, the reader is referred to the Web version of this article.)

spread ones. Nevertheless, the vibrations stemming from the punctual central leak on the one hand and from crack leaks below ground level on the other hand are detected within similar orders of magnitudes, hinting on that for practical purposes and realistic leaks, this potential bias in sensitivity might not be too strong a limitation to locate the most critical regions. Measurements (not reported here) performed on a smaller concrete mock-up [43] with a controlled flow injected into leaks of various kinds (punctual, decimeter long cracks between joints, and highly porous square-decimeter wide areas) confirm this trend.

A finer analysis is however difficult, which is a limitation in making attractive to real applications this way of detecting leaks by only looking at the amplitude distribution. Apart from a broadband component, all points display intensity patterns with maxima and minima that change from point to point, even for those points which appear to be illuminated by the same leaks. For instance, points in the central region have an intensity peak in the low frequency part that changes from 2 kHz (for A41) to 7 kHz (for A43). A similar comment can be made on the A1i sensors. Therefore, these observed peaks may not be attributed to characteristics of the leaks, but must be consequences of the wave propagation inside the structure. As a matter of fact, all strong leaks are located near strong heterogeneities: the leaks at -1 m are close to or at the interface between the wall and the base slab, while those in the central region emit waves which interact with the steel door and the thickness steps of the square concrete sealing. As a consequence, the resulting directivity patterns of the sources can be expected to be quite complex and frequency dependent. Furthermore, most are cracks with a well defined orientation, which also contributes to a complex directivity. Lastly, although it should play a weaker role, even far from the leaks the wall is not perfectly homogeneous as the construction joints between layers (see Fig. 1-(d)) and the thick post-tensioning cables hold by anchoring heads should also act as wave scatterers that produce interference patterns and yield to spatial variations of the vibration field.

The principal result of the 2018 experiment is to give orders of magnitudes for the amplitudes and an estimation of the detection range: despite the weakness of the signals, and despite the noisy background - which could be successfully filtered out due to its very specific nature, the acquisition chain deployed here can allow for a detection of 500–600 L/h leaks at 4–5 m distance in the 2–20 kHz range, thanks to an accumulation of correlations over 2 min long records. But this estimation of a detection distance must be tempered by the fact that amplitude spectra measured far from a source are difficult to interpret due to the complex directivity and interference patterns. For a successful blind usage, it appears necessary to do as if the detection threshold were shorter to avoid missing near-field signatures that are the best evidence of the presence of a leak.

4.2. Analysis of the 2019 experiment

The results of the 2019 experiment are processed according to Eqs. (1) and (2) by averaging over 2 min long records, and the two beamforming methods given in Eqs. (4) and (7) are applied to retrieve the angular positions of the sources. The time delays (6) are constructed by taking as phase velocity that of the fundamental anti-symmetric mode $c = c^{(A_0)}(f)$ (see Fig. 2). The outcomes are represented in Fig. 8. The spectra drawn in Fig. 8-(a), (b) and (c) are averaged over the 8 sensors which constitute the B3, B2 and B1 antennas, and the black vertical lines and arrows indicate the frequency ranges selected for the beamforming analysis. These ranges were chosen to split the bandwidth into several sub-intervals where the performance of both methods is expected to vary. In principle, low frequencies are desirable for long range detection because they attenuate less and are less sensitive to scattering by small obstacles. However, the wave propagation is also more complex at low frequencies (see Sec. 2.3 and below). In Fig. 8-(d)–(h) each antenna is represented by a set of 8 black circles while the solid orange (for $\Delta p = 2$ bars) and green (for $\Delta p = 4.2$ bars) curves drawn around their centers represent the outcome of the applied beamforming formula. For an easier interpretation, direct and specular rays (reflected by the central access door) are traced between each antenna and strong neighboring leaks.

The relation between amplitude and pressure can be observed with more accuracy on this data set in Fig. 8-(a), (b) and (c), although it is focused on one leak and is hence less representative than the 2018 experiment. The quadratic law describes well the dependence from, say, 5 kHz, but the lower frequency part would be better described with a law of smaller exponent.

It is worth recalling a few points concerning the design of the arrays and the wave propagation characteristics (see Secs. 2.2 and 2.3) based on which performances may be expected. Firstly, the inter-sensor spacing within an array is 0.12 m, meaning that the corresponding Nyquist frequency for the surface wave (2400 m/s velocity) around which D&S is supposed to work best is 10 kHz. Below this frequency, the main lobe is less and less resolved – this is the case where MVDR is relevant. On the other hand, secondary lobes start to contaminate the outcome at higher frequencies. Secondly, the wave propagation is noticeably multi-modal between 4 and 10 kHz, an interval where degraded performances are then expected. Above 10 kHz the surface wave dominates the long range out-of-plane motion.

A beamforming analysis is first performed in the 1–3 kHz range (Fig. 8-(d)). This part of the spectra is puzzling for two reasons. Firstly, because the two peaks that appear (Fig. 8-(a), -(b) and (-c)) are unexpected: the only thickness resonances are the A_1 and SH_1 cutoff, whose corresponding modeshapes have zero out-of-plane motion and are therefore not suited to be excited by a through-thickness flow nor to be

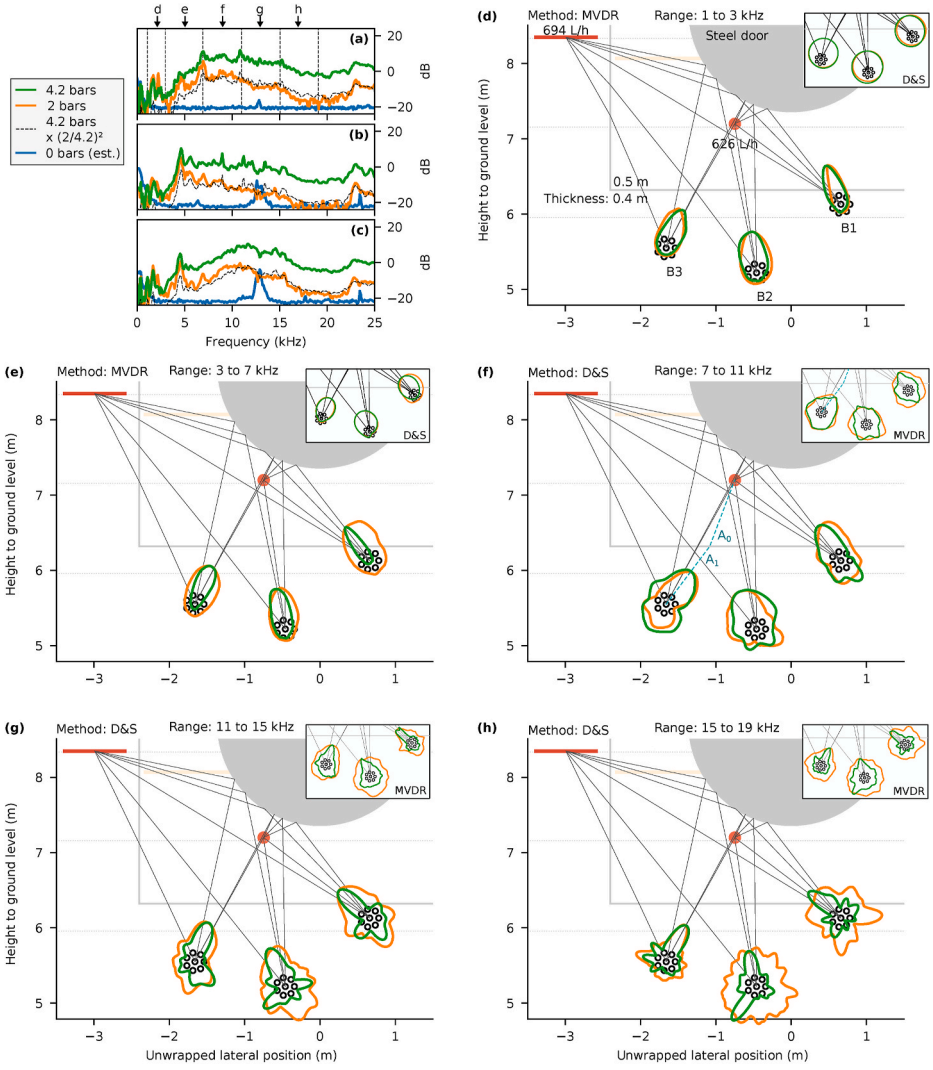

Fig. 8. Results of the 2019 experiment: beamforming (MVDR or D&S) integrated in several frequency ranges. (a), (b) and (c): Average spectra of the (a) B3, (b) B2 and (c) B1 arrays, with vertical dotted lines and black arrows indicating the integration ranges. (d) to (h): Angular plots representing the (normalized) magnitude of the beamforming result for each array. The sensors are represented with black circles. Direct and specular rays originating from the two main neighboring leaks are indicated with gray lines. In (f) a ray refracted by the interface at the wall thickness step is also traced (dotted blue lines) as a possible explanation of an anomalous peak in the beamforming amplitude of the B3 array. (For interpretation of the references to color in this figure legend, the reader is referred to the Web version of this article.)

detected by the sensors used. Second, because the measured amplitude is the same at the 2 bars and 4.2 bars steps. The MVDR beamforming of the B2 array points towards the punctual leak, but the B1 array unambiguously points towards the center of the steel door where there is no known leak. The B3 array is consistent with both. The explanation in which we believe is that this part of the spectrum may be influenced by resonances of the steel door. Indeed, from the dimensions of the door (2.7 m diameter) and typical sound velocities in steel (5900 m/s and 3200 m/s for P- and S-waves), one may expect the lowest resonances to be within this range. The door would then behave as a secondary noise source that would emit radially outgoing waves at these frequencies. The excitation mechanism could be a near field coupling effect with the neighboring point leak. As for the amplitude, we believe that the flow-structure interaction has reached a saturation level, a phenomenon we frequently observe on a smaller mock-up (see previous paragraph) and which we attribute to the triggering of new paths for the flow within the crack.

Other beamforming analyses are done to cover other parts of the spectra (Fig. 8-(e) to -(h)). One can observe how D&S progressively improves in angular resolution while secondary lobes also appear. The MVDR method still yields very satisfactory results in the 3–7 kHz (Fig. 8-(e)) range while the D&S method is more robust at higher frequencies, especially in the $7-11$ kHz range (Fig. 8-(f)) where the propagation is mostly multi-modal. In Fig. 8-(f) a refracted ray corresponding to a $A_0 \rightarrow A_1$ mode conversion at the thickness step is traced[4] as a possible explanation for an anomalous maximum detected by the B3 antenna. The principal information that arises from all this analysis is that the punctual leak direction can be confidently located using either antenna and any part of the spectrum, and this is all one could say in a blind experiment. However, knowing the answer, one can also identify on the B2 and B3 arrays the weaker influence of the horizontal crack leak which is located a bit farther than and has a similar flow rate as the punctual leak. Indeed, in Fig. 8-(f), -(g) and -(h) direct and specular ray directions coincide very well with local maximums of the beamforming amplitudes (see MVDR insets for sharper peaks). These local maximums are often weaker than intensity peaks in other directions and are undoubtedly not sufficient to reveal the horizontal crack, but could be hints to confirm information obtained from antennas installed at other locations in the wall.

[4] The dispersion relation in the 0.5 m thick wall is assumed to be identical to the 0.4 m thick wall under a frequency scaling $f \rightarrow f \times 50/40$. The refracted ray is traced following Fermat's principle.

5. Conclusion

The detectability of vibrations produced by air leaks has been demonstrated using accelerometers in the 0–20 kHz range under conditions that are relevant for leak tests on real containment buildings. A proportional relation between spectral amplitude and squared applied pressure could be observed at most points and on most of the frequency range - except on its lowest part. This dependence means that the detection cannot be unequivocally sensitive to the flow rate, because one large leak should emit larger vibrations than several small ones summing the same flow rate. Hence, interpretation of detected amplitudes should be done cautiously having in mind that secondary peaks in the maps can be caused by regions leaking most.

Regarding the initial objective to detect flow rates from several hundreds L/h, the corresponding raw signals are very weak, with SNR lower than 1 at a few decimeters to meter distance. Nevertheless, under excellent ambient noise conditions such as those that could be achieved during the experiments (in units of the standard gravity better than 8×10^{-9} g in most of the bandwidth for the 2019 experiment and about 5×10^{-8} g successfully filtered out for the 2018 experiment), accumulating noise correlations on long records lead to effectively improve the SNR as much as theory predicts it, allowing for detection thresholds about 500–600 L/h flow rates at $4 - 5$ m distance with 2 min long records, for small sized leaks. As the amplitudes decrease with the square root of distance and the SNR increases with the quarter power of length of records, theoretically, this range can be doubled by averaging over fourfold increased times, *i.e.* 8 min if ambient noise conditions are good enough. We are confident that we could reach such levels in future works. One should mind however that these ranges were established reliably only for small sized leaks. The results of the 2018 experiment give evidence of detection of meter long cracks at several meters distance and are encouraging for future applications, but more data is needed to determine the ranges with accuracy.

Two complementary beamforming techniques were applied on small antennas to retrieve the location of the vibration sources, and their performance were verified in a context of multi-modal propagation and heterogeneities. These two complexities are specific to the present experiment. Indeed, as real walls are three times thicker, the propagation will be predominantly due to the surface wave in almost the entire frequency range of interest. Furthermore, as most of the wall is reasonably homogeneous, phantoms due to multiple paths will be a minor issue.

Before being deployed on real power plants to assist existing techniques, tests on larger scales are needed, with for instance a large portion of the wall being meshed. The purpose is to gain experience on the detectability of leaks that are spread on large cracks, still not sufficiently known. It is also necessary to face technical challenges and costs increases that will emerge from using many sensors – works are ongoing on a dedicated low-cost and low-noise instrumentation with integral electronics. Development of algorithms for on-line processing is another mandatory step to avoid prohibitive amount of data, including a sensitive pre-filter to automatically exclude transient events or treat them separately (as acoustic emission events).

Another direction for future works involving several technical challenges concerns the adaptability of this acoustic method to leak tests on simple walled buildings (made of a thin steel liner covered with a thick concrete wall), which constitute the other half of the french nuclear reactors.

Declaration of competing interest

The authors declare that they have no known competing financial interests or personal relationships that could have appeared to influence the work reported in this paper.

References

[1] Decree No. 2007-1557 of November 2nd, 2007, pertaining to basic nuclear installations and the control, with regard to nuclear security, of the transportation of radioactive materials. in french, https://www.legifrance.gouv.fr/loda/id/JORFTEXT000000469544/2008-07-18/; 2007.

[2] Keogh P. The PWR integrated Leak Rate Test, a review of experiences and results. Nucl Eng Des 1985;90(2):135–41. https://doi.org/10.1016/0029-5493(85)90003-2.

[3] Courtois A, Johnston M, Mortimer R. In: Containment pre-operational tests, in-service inspection and integrated leak rate tests for PWR: a comparison between sizewell B and the EDF French fleet. Manchester, UK: Transactions, SMiRT-23; 2015.

[4] Masson B, Alliard P-M. In: Objectives and design of the new experimental program VeRCoRs based on a 1/3 scaled PWR containment building. Paris, France: TINCE; 2013.

[5] Mathieu J, Charpin L, Sémété P, Toulemonde C, Boulant G, Haelewyn J, Hamon F, Michel-Ponnelle S, Hénault J, Taillade F. Temperature and humidity-driven ageing of the vercors mock-up. In: Computational modelling of concrete structures: proceedings of the conference on computational modelling of concrete and concrete structures, vol. 215. EURO-C 2018); 2018.

[6] Henault J-M, Laviron P, Desforges S, Vautrin D, Courtois A, Martin B, Legrix A. In: How to characterize the air tightness of containment structures. Overview of monitoring techniques tested on VeRCoRs Mock up. Paris, France: TINCE; 2018.

[7] Niepceron J, Corbin M, Masson B. Appraisal of the VERCORS 2018 benchmark. In: Transactions, SMiRT-25; 2019. Charlotte, NC, USA.

[8] Fuchs H, Riehle R. Ten years of experience with leak detection by acoustic signal analysis. Appl Acoust 1991;33(1):1–19. https://doi.org/10.1016/0003-682X(91)90062-J.

[9] Hunaidi O, Chu WT. Acoustical characteristics of leak signals in plastic water distribution pipes. Appl Acoust 1999;58(3):235–54. https://doi.org/10.1016/S0003-682X(99)00013-4.

[10] Gao Y, Brennan M, Joseph P, Muggleton J, Hunaidi O. On the selection of acoustic/vibration sensors for leak detection in plastic water pipes. J Sound Vib 2005;283(3):927–41. https://doi.org/10.1016/j.jsv.2004.05.004.

[11] Murvay P-S, Silea I. A survey on gas leak detection and localization techniques. J Loss Prev Process Ind 2012;25(6):966–73. https://doi.org/10.1016/j.jlp.2012.05.010.

[12] Meng L, Yuxing L, Wuchang W, Juntao F. Experimental study on leak detection and location for gas pipeline based on acoustic method. J Loss Prev Process Ind 2012;25(1):90–102. https://doi.org/10.1016/j.jlp.2011.07.001.

[13] Colombo AF, Lee P, Karney BW. A selective literature review of transient-based leak detection methods. J Hydro-Environ Res 2009;2(4):212–27. https://doi.org/10.1016/j.jher.2009.02.003.

[14] Holland SD, Roberts R, Chimenti DE, Strei M. Leak detection in spacecraft using structure-borne noise with distributed sensors. Appl Phys Lett 2005;86(17):174105. https://doi.org/10.1063/1.1906324.

[15] Holland SD, Roberts R, Chimenti D, Song JH. An ultrasonic array sensor for spacecraft leak direction finding. Ultrasonics 2006;45(1):121–6. https://doi.org/10.1016/j.ultras.2006.07.020.

[16] Holland SD, Chimenti DE, Roberts R, Strei M. Locating air leaks in manned spacecraft using structure-borne noise. J Acoust Soc Am 2007;121(6):3484–92. https://doi.org/10.1121/1.2722051.

[17] Moriot J, Maxit L, Guyader J, Gastaldi O, Périsse J. Use of beamforming for detecting an acoustic source inside a cylindrical shell filled with a heavy fluid. Mech Syst Signal Process 2015;52–53:645–62. https://doi.org/10.1016/j.ymssp.2014.07.022.

[18] Bucker HP. Use of calculated sound fields and matched-field detection to locate sound sources in shallow water. J Acoust Soc Am 1976;59(2):368–73. https://doi.org/10.1121/1.380872.

[19] Baggeroer AB, Kuperman WA, Mikhalevsky PN. An overview of matched field methods in ocean acoustics. IEEE J Ocean Eng 1993;18(4):401–24.

[20] Rost S, Thomas C. Array seismology: methods and applications. Rev Geophys 2002;40(3). https://doi.org/10.1029/2000RG000100. 2–1–2–27.

[21] Corciulo M, Roux P, Campillo M, Dubucq D, Kuperman WA. Multiscale matched-field processing for noise-source localization in exploration geophysics. Geophysics 2012;77(5). https://doi.org/10.1190/geo2011-0438.1. KS33–KS41.

[22] McLaskey GC, Glaser SD, Grosse CU. Beamforming array techniques for acoustic emission monitoring of large concrete structures. J Sound Vib 2010;329(12):2384–94. https://doi.org/10.1016/j.jsv.2009.08.037.

[23] Chehami L, Moulin E, de Rosny J, Prada C, Bou Matar O, Benmeddour F, Assaad J. Detection and localization of a defect in a reverberant plate using acoustic field correlation. J Appl Phys 2014;115(10):104901. https://doi.org/10.1063/1.4867522.

[24] Chehami L, Moulin E, de Rosny J, Prada C, Chatelet E, Lacerra G, Gryllias K, Massi F. Nonlinear secondary noise sources for passive defect detection using ultrasound sensors. J Sound Vib 2017;386:283–94. https://doi.org/10.1016/j.jsv.2016.10.006.

[25] Xenaki A, Gerstoft P, Mosegaard K. Compressive beamforming. J Acoust Soc Am 2014;136(1):260–71. https://doi.org/10.1121/1.4883360.

[26] Gemba KL, Hodgkiss WS, Gerstoft P. Adaptive and compressive matched field processing. J Acoust Soc Am 2017;141(1):92–103. https://doi.org/10.1121/1.4973528.

[27] Niu H, Ozanich E, Gerstoft P. Ship localization in santa barbara channel using machine learning classifiers. J Acoust Soc Am 2017;142(5):EL455–60. https://doi.org/10.1121/1.5010064.

[28] Khan S, Huh J, Ye JC. Adaptive and compressive beamforming using deep learning for medical ultrasound. IEEE Trans Ultrason Ferroelectrics Freq Control 2020;67 (8):1558–72. https://doi.org/10.1109/tuffc.2020.2977202.
[29] Lobkis OI, Weaver RL. On the emergence of the green's function in the correlations of a diffuse field. J Acoust Soc Am 2001;110(6):3011–7. https://doi.org/10.1121/1.1417528.
[30] Derode A, Larose E, Tanter M, de Rosny J, Tourin A, Campillo M, Fink M. Recovering the green's function from field-field correlations in an open scattering medium (l). J Acoust Soc Am 2003;113(6):2973–6. https://doi.org/10.1121/1.1570436.
[31] Shapiro NM, Campillo M, Stehly L, Ritzwoller MH. High-resolution surface-wave tomography from ambient seismic noise. Science 2005;307(5715):1615–8. https://doi.org/10.1126/science.1108339.
[32] Ruigrok E, Gibbons S, Wapenaar K. Cross-correlation beamforming. J Seismol 2016;21(3):495–508. https://doi.org/10.1007/s10950-016-9612-6.
[33] Auld BA. Acoustic fields and waves in solids, vol. II. Wiley; 1973.
[34] Mokhtar TA, Herrmann RB, Russell DR. Seismic velocity and q model for the shallow structure of the arabian shield from short-period Rayleigh waves. Geophysics 1988;53(11):1379–87. https://doi.org/10.1190/1.1442417.
[35] Forbriger T. Inversion of shallow-seismic wavefields: I. wavefield transformation. Geophys J Int 2003;153(3):719–34. https://doi.org/10.1046/j.1365-246x.2003.01929.x.
[36] Carino NJ. The impact-echo method: an overview, vol. 15; 2001. p. 1–18. https://doi.org/10.1061/40558.
[37] Gibson A, Popovics JS. Lamb wave basis for impact-echo method analysis. J Eng Mech 2005;131(4):438–43. https://doi.org/10.1061/(ASCE)0733-9399(2005)131:4(438).
[38] Prada C, Clorennec D, Royer Da. Local vibration of an elastic plate and zero-group velocity lamb modes. J Acoust Soc Am 2008;124(1):203–12. https://doi.org/10.1121/1.2918543.
[39] Oppenheim AV, Schafer RW. Digital signal processing. Englewood Cliffs, NJ: Prentice-Hall; 1975.
[40] Bartlett MS. Smoothing periodograms from time-series with continuous spectra. Nature 1948;161(4096):686–7. https://doi.org/10.1038/161686a0.
[41] Bartlett MS. Periodogram analysis and continuous spectra. Biometrika 1950;37(1/2):1. https://doi.org/10.2307/2332141.
[42] Capon J. High-resolution frequency-wavenumber spectrum analysis. Proc IEEE 1969;57(8):1408–18.
[43] Vautrin D, d'Urso G. Tests on acquisition chains ACOEM et OSEAN for the detection of leaks by acoustic methods. In: Tech. Rep. 6125-3117-2019-00009-FR, EDF R&D. Chatou, France: PRISME Department; 2019. in french.